Journal of Geophysical Research

Supporting Information for

The impact of a 3-D Earth structure on glacial isostatic adjustment in Southeast Alaska following the Little Ice Age

C.P. Marsman[1,2,3], W. van der Wal[1,2], R.E.M. Riva[1], J.T. Freymueller[4]

[1]Faculty of Civil Engineering and Geosciences, Delft University of Technology, Delft, the Netherlands

[2]Faculty of Aerospace Engineering, Delft University of Technology, Delft, the Netherlands

[3]Now at Department of Earth Sciences, Utrecht University, Utrecht, the Netherlands

[4]Department of Earth and Environmental Sciences, Michigan State University, East Lansing, MU, USA

Contents of this file

1. Benchmark for a 3D GIA model in SE-Alaska

The validity of the finite element code is checked with the output obtained by a normal-mode model in Hu and Freymueller (2019). The benchmark model consists of 5 unique material layers, which are defined in Table S1.

Table S1: Material properties of the incompressible 5-layered Earth model.

Top of layer radius (km)	Layer thickness (km)	Density (kg/m^3)	Young's modulus (GPa)	Poisson's ratio (-)	Viscosity Pa-s	Gravity (m/s^2)
6371	55	3028.4	157.6	0.4999	-	9.761
6361	230	3397.8	209.0	0.4999	3.00×10^{19}	9.794
6086	385	3729.3	288.9	0.4999	2.40×10^{21}	9.873
5701	2221	4877.9	658.4	0.4999	5.01×10^{21}	9.963
3480	3480	10931.7	-	-		10.629

The number of finite elements required per Earth layer was investigated in order to minimize the bending errors associated with using linear finite elements. The first test included two finite element layers per Earth layer. The calibration test showed this setup resulted in lower uplift rates, indicating that the FE model does not bend enough. The second test included a total of 26 finite element layers, where the layer thickness increases with increasing depth, as shown in Table S2

Table S2: Finite element layers definition. *FE layer thicknesses are given from top to bottom layer.

Earth layer top radius (km)	Thickness (km)	Number of FE layers	FE layer thicknesses* (km)
6371	55	4	12, 14, 14, 15
6361	230	11	15, 9x20, 35
6086	385	4	55,60,135,135
5701	2221	6	2x250, 3x430, 431
3480	3480	1	3480

We tested the horizontal element size to as well. The ice model is made of disks of approximately 22 km diameter (0.2°). The normal-mode model in Hu and Freymueller (2019) uses spherical harmonics with maximum order and degree 2048 (~10 km resolution). Tests were performed using 10 and 15 km element sizes. The 10 km resolution test did not yield significantly better results than the 15 km resolution test (differences less than 0.5 mm/yr) and resulted in much longer computational times. For that reason, the 15 km resolution was used in further simulations as it was adequate to represent the observed deformation.

The uplift rates (averaged between 2003 and 2012) for all of Alaska for both the normal-mode (NM) and finite element (FE) models can be seen in Figure S1. The uplift patterns obtained by both models are remarkably similar, indicating that FE model accuracy limitations and the absence of self-gravity and sphericity do not impact the results. Next, we will study the differences in Southeast Alaska interpolated at the GPS stations.

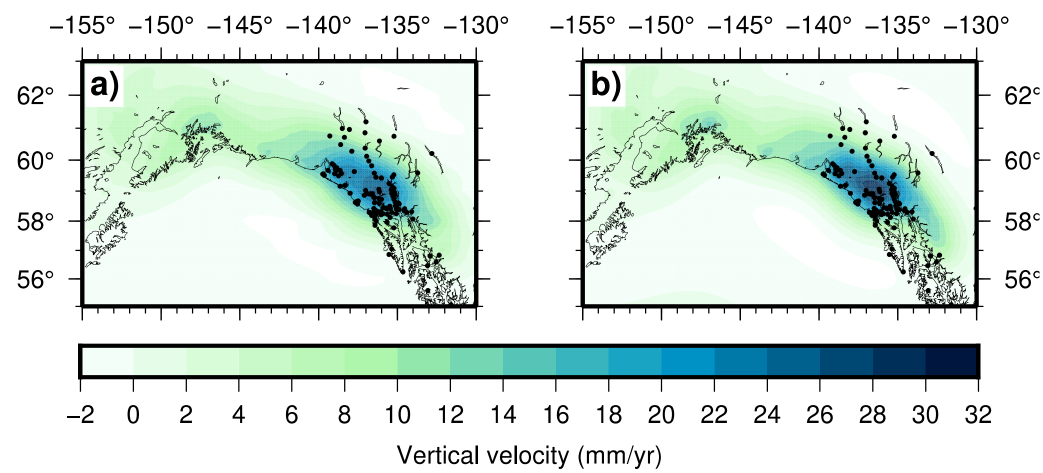

Figure S1: averaged uplift rates between 2003-2012 for (a) the spherical NM model and (b) the flat Earth FE model. Black dots indicate GPS locations.

The interpolated differences at the GPS locations between the uplift rates and the two models and their histograms are depicted in Figure S2. The differences vary between 0.5 and 2.5 mm/yr. The largest differences (>1 mm/yr) correspond to the Yakutat Icefields, where the load changes are very large; the model differences there still represent <10% of the signal. Note that regions outside Southeast Alaska are not included in this statistical analysis, as differences between the two models are close to zero outside this region. The relatively larger magnitude in the Yakutat Icefields is likely due to the enhanced ice loss modelled for this area, which leads to larger differences in the relaxation times between the FE and NM models. In addition, the enhanced ice loss in this area is implemented with an increase in ice loss rate at three disks in the spherical model (Hu &

Freymueller, 2019) which is smoothed in the finite element model. Overall, the remaining differences between the normal-mode and finite element models are due to a number of factors, which include (i) discretization of the ice model, (ii) fundamental differences between the two methods, such as neglect of sphericity and self-gravitation in the FE model, resulting in different relaxation times.

The models are tested against the observational data, using a Chi-square (χ^2) test. The Chi-square values for the FE and NM models are 17.7 and 17.2, respectively, which are relatively close to each other. Note that the prior value is larger in the main text, as the model performance was tested against the GPS dataset in Hu and Freymueller (2019) which has fewer measurement points in comparison to the dataset used in the main text.

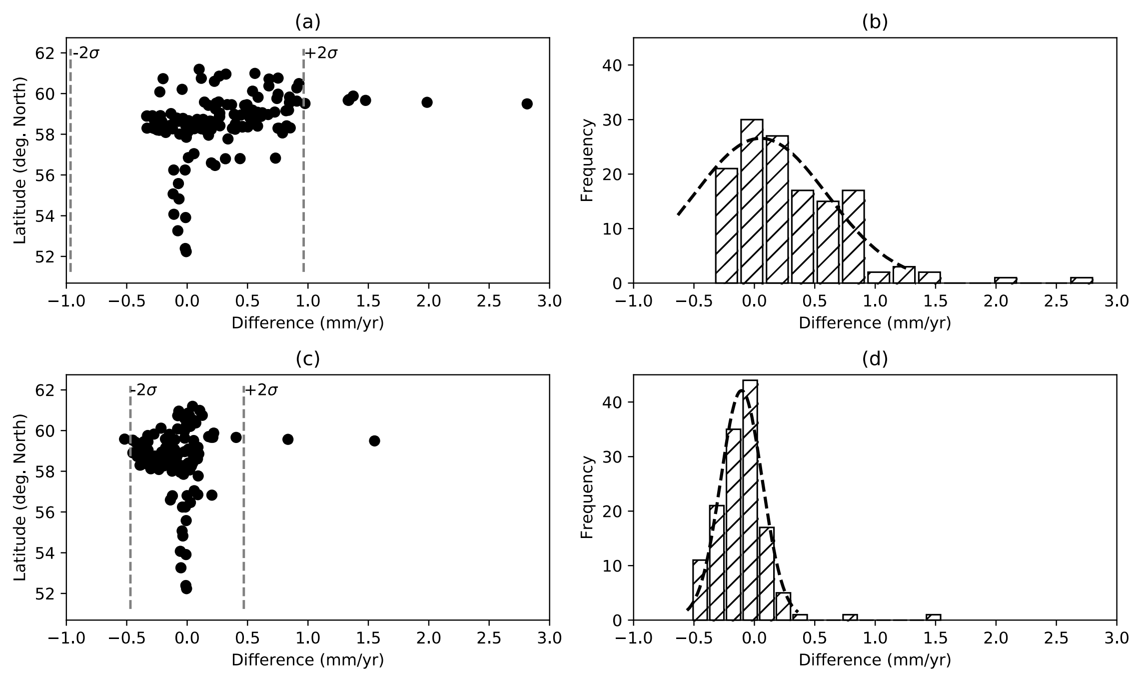

Figure S2: Differences in uplift between the finite element and normal-mode models and their histograms. (a), (b) and (c), (d) correspond to the periods 1995-2003 and 2003-2012, respectively. The dotted curves in (b) and (d) are fitted to a Gaussian distribution covering the 95% confidence interval. Only the viscoelastic response since the LIA is modelled here.

2. The olivine flow law approach

In this section, the methodology in van der Wal et al. (2013) is used to retrieve creep parameters. We assume that the main constituent of the mantle material up to 400 km depth is olivine (Turcotte

& Schubert, 2002) and assume this controls the deformation in the mantle. Diffusion creep and dislocation creep are described using a general flow law for olivine, where the strain rate depends on stress to a certain power (Hirth & Kohlstedt, 2004):

$$\dot{\varepsilon} = A\sigma^{n} d^{-p} f H_2O^{r} e^{-\frac{E+PV}{RT}} \, , \tag{1}$$

where $\dot{\varepsilon}$ is the strain rate, A is a constant, σ the induced stress to a power n, d the grain size to a power $-p$, H_2O the water content to a power r, E the activation energy, P the pressure, R, the gas constant, and T the absolute temperature. Note that partial melt is ignored in this study and omitted from Equation 1. In case of diffusion creep, a linear relation exists between the stress and strain rate, and thus the power is 1. For dislocation creep, the problem becomes non-linear, where the power law exponent *n* is approximately 3.5 (e.g.Whitehouse, 2018).

Diffusion and dislocation creep parameters are assigned to each FE element (B_{diff} and B_{diff}) and the effective viscosity can be computed with (van der Wal et al., 2013):

$$\eta_{eff} = \frac{1}{3B_{diff} + 3B_{disl}q^{n-1}} \, , \tag{2}$$

where B_{diff} and B_{disl} are the diffusion and dislocation creep parameters, respectively, and $q = \sqrt{\frac{3}{2}\sigma'_{ij}\sigma'_{ij}}$ is the Von Mises stress in which σ'_{ij} is an element of the deviatoric stress tensor. The *B* parameters contain the parameters in Equation 2 such that $B = \; Ad^{-p} f H_2O^{r} e^{-\frac{E+PV}{RT}}$. In this study only diffusion creep is considered as the stress state in the mantle is poorly known, so the contribution of dislocation creep to the effective viscosity is unclear. In presence of large background tectonic stresses, the stress changes due to GIA have only a small effect on the effective viscosity (van der Wal et al., 2013) and the GIA process is effectively linear (Schmidt, 2012). This makes the diffusion creep model adequate, although the inferred grain size or other adjustable parameter values could be biased if there is a substantial effect due to dislocation creep. The input parameters for the creep parameters are taken from Hirth and Kohlstedt (2004), which are depicted in Table S3. Note that the pre-factor *A* for wet rheologies is reduced by a factor 3 as done in M. Behn et al. (2008) and Freed et al. (2012) due to calibration for water content in olivine (Bell et al., 2003).

Table S3: Rheological parameters for diffusion creep mechanisms for wet and dry rheology settings. Values from Hirth and Kohlstedt (2004). [a]The pre-factor A for wet rheologies in reduced by a factor 3 following M. D. Behn et al. (2009); Freed et al. (2012) due to calibration for water content in olivine.

No.	A	E (kJ/mol)	V (10^{-6} m^3/mol)	r	n	p	Wet/dry
1	1.5E9	375	5	-	1	3	Dry
2	[a]3.33E5	335	4	1	1	3	Wet

The viscosity profiles are tuned with the grain size and water content, which do not vary laterally or with depth. Lateral and depth variations in the 3-D viscosity model thus result from variations in temperature. Partial melt is ignored in this study, but may be important in select local areas beneath volcanic zones (Hyndman, 2017). Typical grain sizes found in peridotite-gabbros in Southeastern Alaska are 1-4 mm (Himmelberg & Loney, 1986; Himmelberg et al., 1986) but can lead up to 10 mm (Morales & Tommasi, 2011), hence the grain size in this study is varied between 1-10 mm. Both dry and wet rheology settings are considered. However, there is a preference for a wet rheology setting. Laboratory experiments show that the presence of water significantly weakens the olivine material (Hirth & Kohlstedt, 2004). In Dixon et al. (2004) evidence is shown for low viscosities beneath western Unites States, which are attributed to the subducting oceanic plate hydrating the upper mantle.

Temperatures are taken from WINTERC-G (Fullea et al., 2021), a global reference temperature model. The averaged temperature profile underneath Southeast Alaska from interpolated values of WINTERC-G are shown in Figure 3 in the main text along with temperature profiles by Hyndman et al. (2009) (regional) and Stacey and Davis (2008) (global average). The temperature profile by Stacey and Davis (2008) is not representative of Southeast Alaska as its geotherm follows a much older and thus thicker thermal lithosphere. The shallow upper mantle temperatures are thus too low and as a result, viscosities would be higher. The temperature profile obtained with WINTERC-G shows high temperatures and a thermal lithospheric thickness of approximately 90 km. A regional study by Hyndman et al. (2009) computed the temperatures from the NA04 North American shear wave velocity model (van der Lee & Frederiksen, 2005) following the method by Goes et al. (2000). Hyndman et al. (2009) incorporated a thermally dependent anelastic correction, resulting in lower temperatures. The thermal lithosphere is approximately 60 km and below it follows the adiabatic gradient approximately. When comparing the regional study with the WINTERC-G profile, it seems that temperatures by WINTERC-G are overestimated. Differences can be explained due to the different shear wave velocity models, methods and compositions used. Neglecting the importance of anelastic effects in a high temperature region could lead to higher temperatures in WINTERC-G. Moreover, both models do not include effects of water content or partial melt. Both parameters cause a reduction in seismic velocities and temperatures could be overestimated (Hyndman et al., 2009). Hyndman et al. (2009) estimates that their estimated temperatures could be 50ºC too high for the Cordillera if the mantle is significantly hydrated.

Supplementary figures

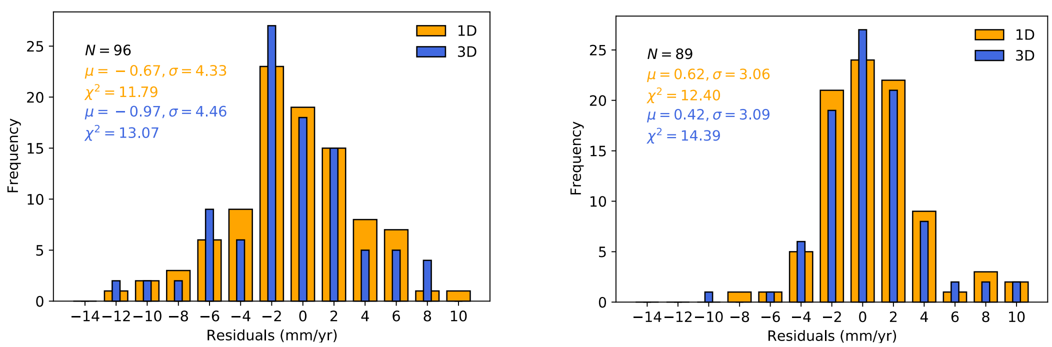

(a) (b)

Figure S3: (a) residual histograms of the 1-D averaged and best fit 3-D model for 1992-2003; (b) the same as (c) but for 2003-2012.

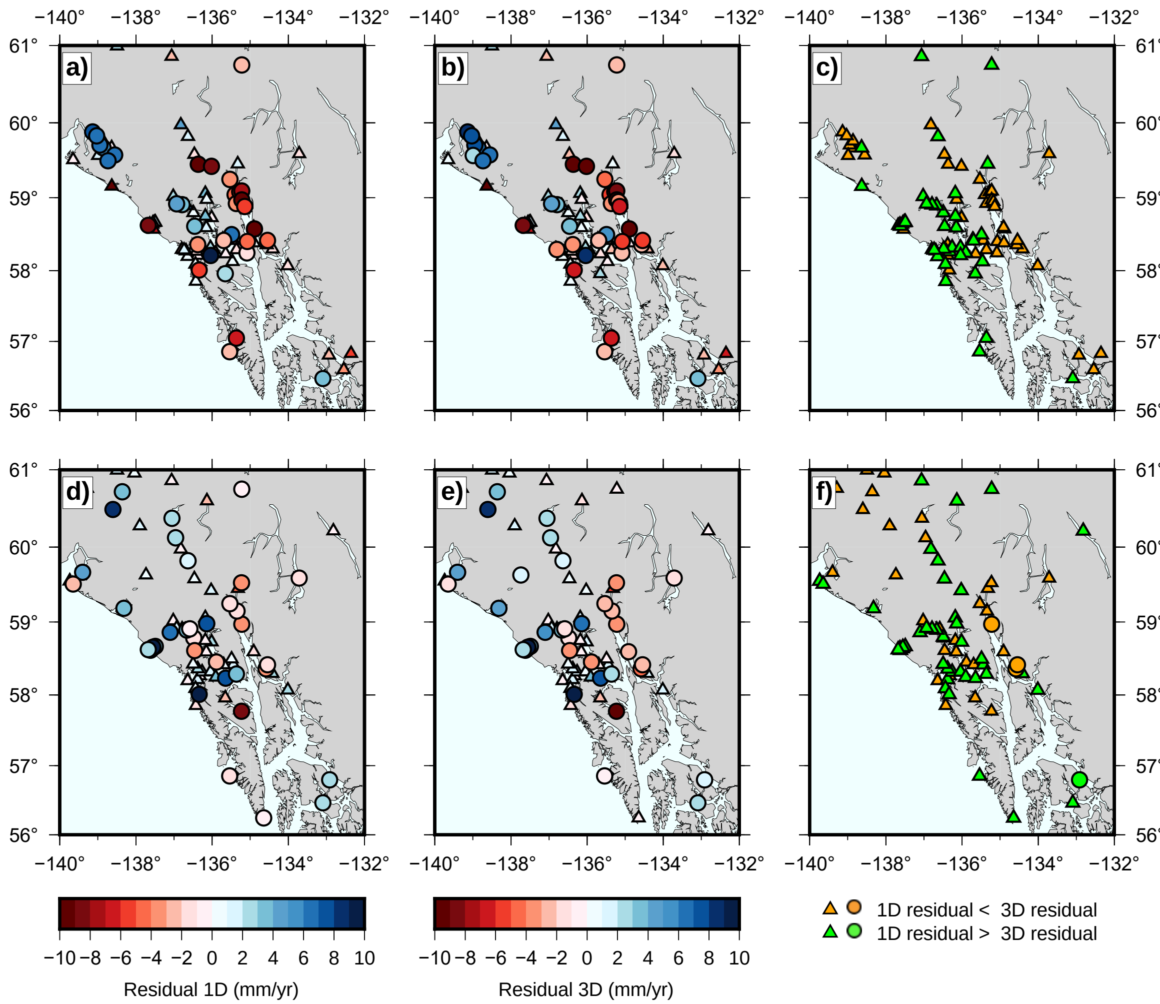

Figure S4: (a) residuals of the uplift predictions between 1992-2003 of the best fit 3-D model; (b) residuals of the uplift predictions between 1992-2003 of the best fit averaged 1-D model; (c) indications at which location the 3-D model residuals are larger or smaller than the 1-D model residuals between 1992-2003; (d) residuals of the uplift predictions between 2003-2012 of the best fit 3-D model; (e) residuals of the uplift predictions between 2003-2012 of the best fit averaged 1-D model; (f) indications at which location the 3-D model residuals are larger or smaller than the 1-D model residuals between 2003-2012.

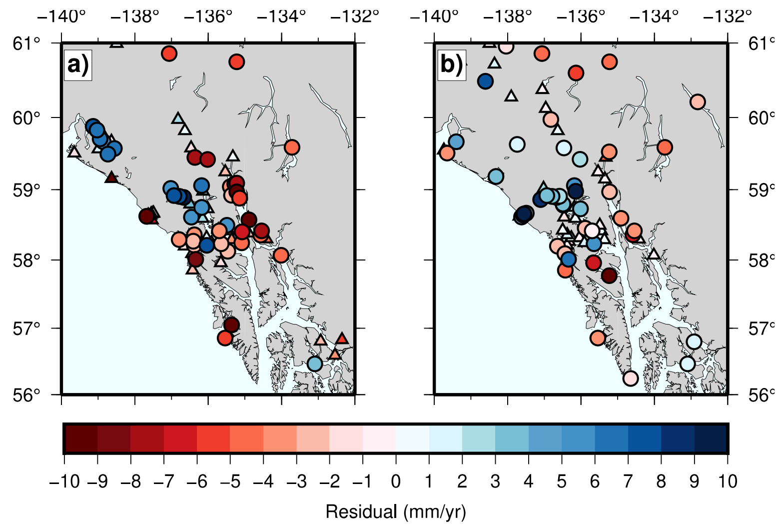

Figure S5: Residuals of the best fit (χ^2=20.7) 3-D model obtained with the flow law approach. a) residuals between 1992-2003; and b) residuals between 2003-2012. The predicted uplift rate is too low (5-10 mm/yr) for both GB and YK. This results from the thick lithosphere prescribed by the temperature model.

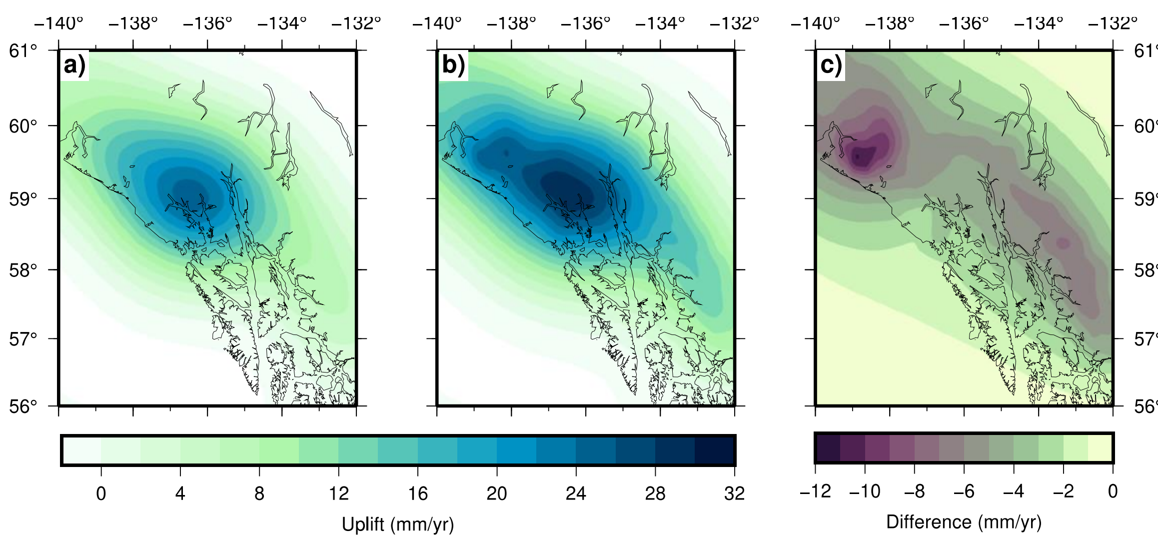

Figure S6: Average uplift rate (2003-2013) for (a) where the ice loading ends 1995 and (b) where the ice loading ends in 2012. In (c) the differences between (a) and (b) are plotted. The differences represent an approximation of the elastic response. We estimate the PDIM effects around the Yakutat Icefields and Glacier Bay account for approximately 45-50% and 25% of the uplift caused by the viscoelastic response (LIA and PDIM). Larsen et al. (2005) predicted that the elastic uplift rates account for 40% and 15% of the observed uplift near the Yakutat Icefields and Glacier Bay, respectively. The larger predictions here are due to the enhanced ice loss modelled.